ORIGINAL ARTICLE

Automated segmentation and detection of increased uptake regions in bone scintigraphy using SPECT/CT images

Masakazu Tsujimoto[1] · Atsushi Teramoto[2] · Seiichiro Ota[3] · Hiroshi Toyama[3] · Hiroshi Fujita[4]

Abstract

Purpose To develop a method for automated detection of highly integrated sites in SPECT images using bone information obtained from CT images in bone scintigraphy.

Methods Bone regions on CT images were first extracted, and bones were identified by segmenting multiple regions. Next, regions corresponding to the bone regions on SPECT images were extracted based on the bone regions on CT images. Subsequently, increased uptake regions were extracted from the SPECT image using thresholding and three-dimensional labeling. Last, the ratio of increased uptake regions to all bone regions was calculated and expressed as a quantitative index. To verify the efficacy of this method, a basic assessment was performed using phantom and clinical data.

Results The results of this analytical method using phantoms created by changing the radioactive concentrations indicated that regions of increased uptake were detected regardless of the radioactive concentration. Assessments using clinical data indicated that detection sensitivity for increased uptake regions was 71% and that the correlation between manual measurements and automated measurements was significant (correlation coefficient 0.868).

Conclusion These results suggested that automated detection of increased uptake regions on SPECT images using bone information obtained from CT images would be possible.

Keywords Bone scintigraphy · SPECT/CT · Image processing · Bone metastasis

Introduction

Bone metastasis can occur in all types of cancer; therefore, during routine care of cancer patients, it is necessary to pay particular attention to signs of bone metastasis to determine the appropriate treatment strategy [1]. Bone scintigraphy has long been used to diagnose bone metastasis. It has a particularly high sensitivity to osteogenic types of cancer, such as prostate and breast cancers, and thus remains an important diagnostic tool [2–6].

Previously, the interpretation of images obtained by bone scintigraphy required whole-body anterior and posterior images which were acquired as two-dimensional (2D) images by projecting the three-dimensional (3D) structure of the bones in each direction. When 2D images are used, overlapping, scattering, and attenuation are unavoidable problems. In addition, because it is necessary to account for the physiological volume of organs, such as the kidneys and bladder, readers with a sufficient amount of skill and experience are required to make accurate diagnoses. Therefore, rather than relying only on anterior and posterior images to make diagnoses, the use of single-photon emission computed tomography (SPECT) images helps to resolve these problems when making diagnoses and has also been reported to improve specificity [7, 8]. In recent years, the use of SPECT/CT, which allows the simultaneous acquisition of both SPECT and CT images, has facilitated the acquisition of highly precise whole-body SPECT images with attenuation correction using CT images. Consequently, this has

✉ Masakazu Tsujimoto
mckz-t@fujita-hu.ac.jp

1　Department of Radiology, Fujita Health University Hospital, 1-98 Dengakugakubo, Kutsukake, Toyoake, Aichi 470-1192, Japan

2　Faculty of Radiological Technology, School of Health Sciences, Fujita Health University, Toyoake, Japan

3　Department of Radiology, School of Medicine, Fujita Health University, Toyoake, Japan

4　Department of Electrical, Electronic and Computer Engineering, Faculty of Engineering, Gifu University, Gifu, Japan

enabled 3D assessments of even regions known to be difficult to diagnose.

Diagnoses using bone scintigraphy are dependent mainly on the subjective assessment of the physician. Problems with subjective assessments include the fact that they lack objectivity when diagnosing regions of increased uptake [9]. Erdi et al. proposed a method of quantitatively assessing increased uptake on bone scintigraphy using the bone scan index (BSI) [10]. Sadik et al. developed a method of automated analysis of individual increased uptake regions that recognized different bones of the skeleton on whole-body planar images in bone scintigraphy [11–13] and proposed a method of automated calculation of BSI [9]. These techniques are already being used in clinical settings [14]. However, these existing techniques use 2D images for image analysis, and no method of 3D analysis using whole-body SPECT/CT images has yet been proposed. The use of SPECT/CT images allows the analysis of increased uptake regions on SPECT images while simultaneously utilizing the bone information obtained from CT images and represents a major improvement over conventional methods that utilize 2D images. In this study, we propose a novel automated method of analyzing regions of increased uptake regions using SPECT/CT images.

Materials and methods

Overview of the image processing technique

Figure 1 shows a flowchart overview of our method. Bone regions were extracted from CT images, increased uptake regions on SPECT images corresponding to those regions on CT images were identified, and the ratio of increased uptake regions to all bone regions was obtained.
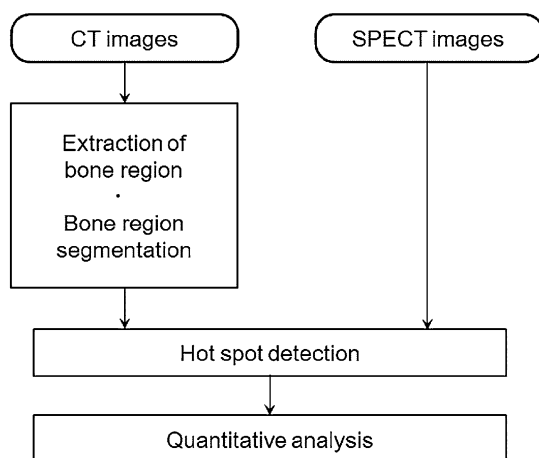

Fig. 1 Flow of automated detection of increased uptake regions using SPECT/CT images

Bone extraction and segmentation using CT images

In this study, we quantified bone uptake, to accurately detect which, it is first necessary to identify the bone regions. In addition, because bone uptake differs according to specific site, it is necessary to broadly classify different bone regions for the purpose of accurate handling. Therefore, we classified the skeleton into seven regions (head, spine, upper limbs, sternum, ribs, pelvis, and femur) by extracting each bone region from CT images as described below.

Extraction of bone regions

To extract bone regions from CT images, we used the established threshold Th_{bone} to perform thresholding. Using closing processing [15, 16], deficit made through thresholding inside the bone structure was processed to fuse with the bone region. Hereafter, CT images to which these processing procedures were applied are referred to as bone region CT images.

Calculation of bone volume

The bone volume of the entire body was calculated from the extracted bone regions. Because the extent of imaging that can be performed differs for each patient, to standardize the range of the calculations for the target data, the parietal slice $S_{parietal}$ (Fig. 2a ①) and the pelvic lower margin slice S_{pelvis} (Fig. 2a ④) on the transaxial plane of the original CT image were manually indicated. The volume was then calculated within the indicated scope.

Segmentation of the bone regions

Because bone metabolism varies depending upon the specific site, it is necessary to segment SPECT images into multiple regions prior to assessment. Therefore, we divided the skeleton into seven regions from the parietal region to the femur: head, spine, ribs, upper limbs, sternum, pelvis, and femur.

Our method for extracting regions was as follows. The three axes (x, y, and z) used in extraction were defined as anatomical axes; x-axes indicated left–right, y-axes indicated anteroposterior, and z-axes indicated craniocaudal. The parietal ($S_{parietal}$) and pelvis (S_{pelvis}) slice locations were indicated manually on the transaxial plane. In addition, the upper spine (S_{upper}; Fig. 2a ②) and lower spine (S_{lower}; Fig. 2a ③) were also indicated.

Spine: We performed opening processing using an ellipsoid filter extended only in the superior to inferior direction on the bone region CT images containing the slice areas
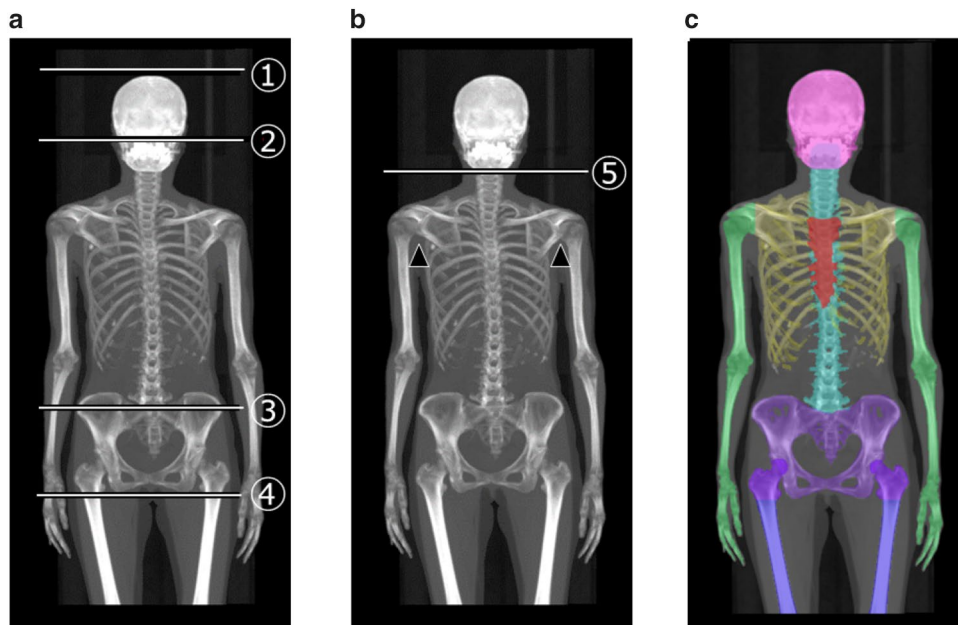
Fig. 2 Bone region segmentation. **a** Manually indicated slice locations. Four slice locations are manually set as anatomical landmarks. Line ①, parietal ($S_{parietal}$); line ②, upper spinal (S_{upper}); line ③, lower spinal (Slower); line ④ lower margin of pelvis (S_{pelvis}). **b** Head and upper limb extraction procedure. Automatically set landmarks in the process of extracting head and upper limbs. Line ⑤ represents the assumed location of the mandible for the purpose of restricting the range to the head. The two arrows (▶) indicate the coordinates of the axilla automatically calculated to identify the upper limbs. **c** Output images of the seven segmented regions. By performing all extraction processes, we segment the seven regions from the whole-body bone regions on CT images

that included the spine to remove he ribs and many bones extending along the *x–y* cross-section. The pixels that underwent opening processing were labeled, and then the spine region alone could be extracted as a rod-shaped structure by selecting only the region with the maximum volume. Next, structures, such as the vertebral arches and spinous processes that were lost due to the previously performed processes were dilated using a maximum filter to fuse them with the spine region. Subsequently, the image that underwent dilation was used as the mask image so that only the spine region (Fig. 2c, light blue-colored area) could be extracted by masking the original image on the bone region CT image.

Head: To restrict the range of the assessment region of the head on the transaxial cross-section to the range from the mandible to the parietal region, we estimated that the slice position S_{chin} would be caudal to the mandible. When designating the distance between the parietal and upper spine slices ($S_{parietal}$–S_{upper}) as L, S_{chin} was designated as follows: $S_{chin} = S_{upper} + L$. Next, we extracted the bone region within the slice area that was superior to S_{chin} from the whole-body bone region CT image. Last, by differentiating the spine from that image, we obtained a head region that included the range from the parietal region to the mandible (Fig. 2c, pink-colored area).

Upper limbs: We performed maximum projection on the y-axis of the bone region CT image. Next, we then extracted the profile curve for the number of pixels on the *x*-axis. We performed second-order differentials on the profile curve that we calculated for the *x*-axis. Using the waveforms thus obtained, we identified the axilla by calculating the zero-crossing along the x-axis from the right and left edges toward the center (Fig. 2b the arrow). We then separated the trunk and upper limbs on the bone region CT image based on the x-coordinate of the armpit that we identified (Fig. 2c, green-colored area).

Pelvis and femurs: We differentiated the head, spine, and upper limb regions that were extracted from the bone region CT image. We then labeled the remaining differential image and identified the region inferior to the lower margin of the pelvis as the region of the femurs (Fig. 2c, blue-colored areas) and the region superior to this margin as the region of the pelvis (Fig. 2c, purple-colored area).

Sternum and ribs: We differentiated the five regions previously extracted from the bone region CT image and obtained only the sternum and rib region image. We then performed opening processing to separate the ribs from each other. Next, we performed thresholding using the fixed value Th_{chest} to obtain the sternum region (Fig. 2c, red-colored area). By differentiating the sternum and rib regions, we extracted only the rib region (Fig. 2c, green-colored area).

SPECT image conversion

SPECT and CT images acquired using the SPECT/CT device are often different in terms of pixel sizes and imaging ranges. When analyzing two types of images, the differences between the two must be compensated for. First, using the bilinear method [15], the pixel size of the SPECT image was aligned with the pixel size of CT images. Next, we compensated for the imaging ranges.

SPECT image standardization

The pixel value of SPECT images changes according to the tracer injection doses, physique of the patient, and amount of urine excreted. To ascertain uptake in the bones more quantitatively, the following equation (Eq. (1)) was used to compensate for the pixel value $I_{\mathrm{SPECT}}(x, y, z)$ of SPECT images, and thereby obtain $I'_{\mathrm{SPECT}}(x, y, z)$. N_b represents the number of pixels in the bone regions obtained from the CT image and C_b represents the total pixel value for the SPECT image calculated within the bone region,

$$I'_{\mathrm{SPECT}}(x, y, z) = \frac{I_{\mathrm{SPECT}}(x, y, z)}{C_b / N_b}. \tag{1}$$

Detection of increased uptake regions

We detected increased uptake regions on SPECT images using thresholding. The threshold value was automatically determined for each patient and region using the mean SPECT count value and standard deviation (SD). Threshold values for detecting increased uptake regions in each patient and region were estimated by multiple regression. The objective variables were threshold values set for evaluating individual accumulation of image data of 13 cases previously having abnormal accumulation by two nuclear medicine specialists. The explanatory variables were the average SPECT count value and standard deviation in each region. Images obtained in the detection of increased uptake regions are shown in Fig. 3.

Elimination of physiological uptake regions

CT images extracted from each region were used as mask images while masking SPECT images, which allowed us to obtain metabolic data from only the seven bone regions of SPECT images. In bone scintigraphy, physiological uptake occurs in organs, such as the kidneys and urinary bladder, but by restricting the scope of images to the bone regions
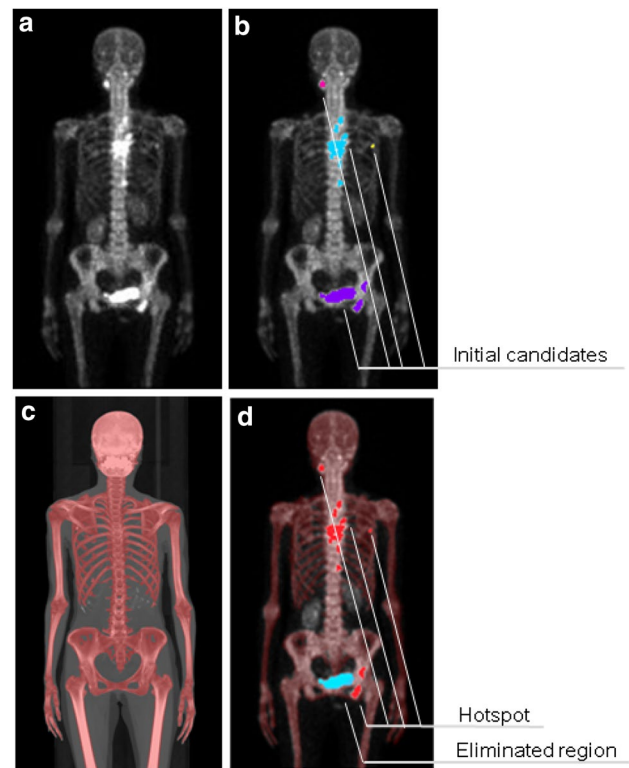

Fig. 3 Initial detection of increased uptake regions on SPECT images and exclusion of physiological uptake using CT images. **a** Original images, **b** initial candidates for increased uptake regions, **c** bone regions (red), and **d** results of masking

only, physiological uptake in regions other than the bones is automatically excluded.

Calculation of the quantitative analysis index

The detected volumes of the increased uptake regions extracted from each region were integrated. The volumetric index (VI), which was used as the 3D analysis index using the volume values detected for the increased uptake regions obtained from SPECT images and the volume values of the bone regions of the whole body extracted from the CT images, was defined using Eq. (2) shown below. VI indicates the volume ratio of the regions of abnormal uptake compared with the whole body. If the uptake is normal, VI is 0. However, as the region of abnormal uptake increases in size compared with the entire body, this value approaches 1. When the imaging range of the whole-body SPECT/CT image did not include the entire body from the parietal region to the toes, the range that was imaged was set as the analytical target of VI,

$$\mathrm{VI} = \frac{\text{Bone volume of the abnormal uptake}}{\text{Bone volume of whole body}}. \tag{2}$$

Evaluation using phantoms and clinical data

We used phantoms and clinical data to assess the efficacy of this method. Data acquisition and image reconstruction in both cases were performed using SPECT/CT device (Symbia T6, Siemens, Germany) and Syngo MI Applications 2009A image processor. We developed our own software using Visual C++ (Microsoft). The softwares Image J and Falcon (version 1.02.420, Nihon Medi-Physics Co., Ltd.) were used for image analysis.

Acquisition conditions of SPECT images were as follows: the number of matrixes was $128 \times 128 \times 224$, pixel size was $4.80 \times 4.80 \times 4.80$ mm^3, enlargement was $\times 1$, and the energy window was 140 keV $\pm$ 15%. The angle of the detector was 180°, number of projections per detector 36, and scan time 10 s per view. Data were obtained using a low-energy high-resolution collimator at the closest orbit. SPECT image reconstruction was performed using Flash 3D in a reconstruction algorithm. Processing was done without scatter correction and with attenuation correction using CT images. The number of iterations was 8, the number of subsets was 9, and the Gaussian filter half width was set at 9.6 mm.

Acquisition conditions of CT images were as follows: the number of matrixes was $512 \times 512 \times 373$, pixel size

$1.27 \times 1.27 \times 5.00$ mm^3, tube voltage 130 kV, reference mAs value 50 mAs (Caredose4D type: AEC + DOM), rotation time was 0.6 s, and helical pitch 1.0. For CT image reconstruction, slice thickness was set at 5.0 mm, and recon increment was 3.0 mm. B08s SPECTAC was used in the reconstruction function.

Evaluation using phantoms

To perform a preliminary assessment of this technique, we prepared a simulated spine phantom composed of a simulated lung phantom and three spine phantoms. An overview is provided in Fig. 4a.

The lung equivalent material was sponge, and the bone equivalent material was dipotassium hydrogen phosphate solution [17]. The concentration of the dipotassium hydrogen phosphate solution was 131.4 mg/mL (CT value 200) and was determined based on the CT values of bones obtained via imaging of a human body phantom (Kyoto Kagaku Co., Ltd.). The simulated spine phantom was composed of three acrylic cylindrical containers. The volume was 36 mm in diameter and 25 mm in length. Because the radioactive concentration for normal spine was 47 kBq/mL, ^{99m}TcO$_4^-$ solution was placed within the bone phantom.

Fig. 4 Evaluation using phantom. **a** Structure of simulated spine phantom. **b** Images resulting from phantoms.
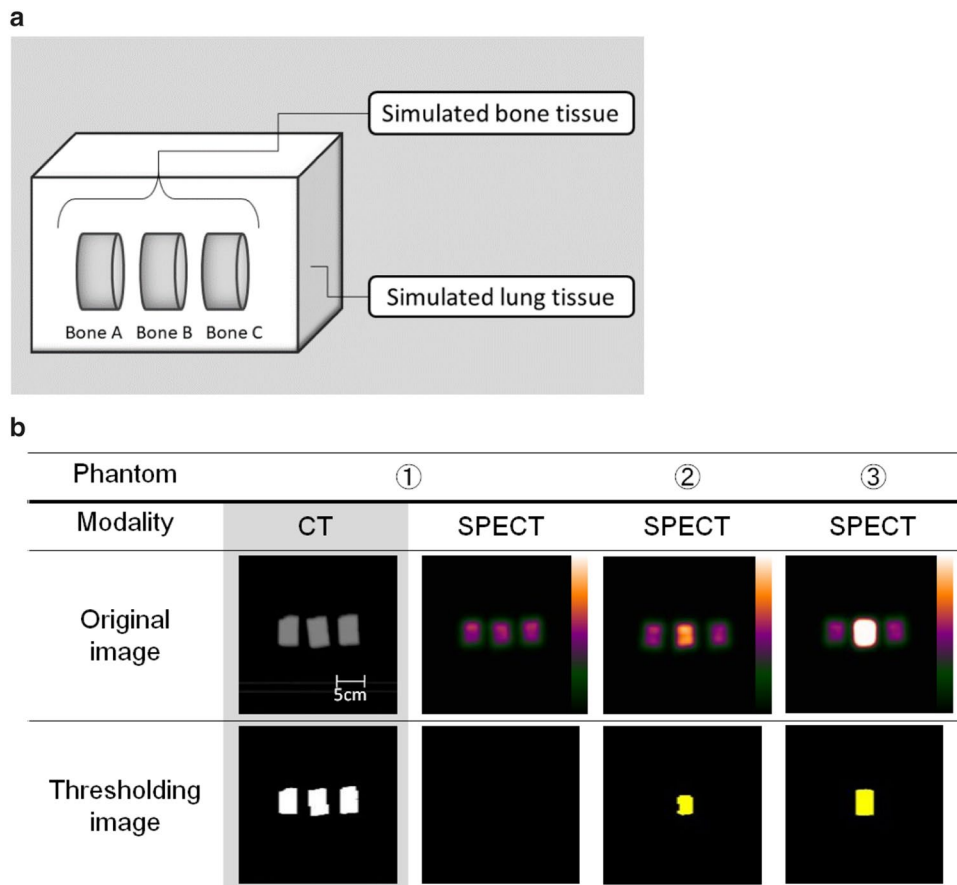
For the three bone phantoms constructed (Bone A–C), only Bone B was subjected to three different radioactivities (phantom number ① to ③; normal = 47 kBq/mL, 1.5 times normal = 70.5 kBq/mL, and 3.7 times normal = 173.9 kBq/mL). The radioactive concentrations placed within Bones A–C were determined based on clinical data (20 normal cases, four cases with typical findings of bone metastasis). The SPECT/CT image acquisition was performed using the simulated bone phantoms (Phantom number ① to ③), and the technique we developed was applied to the images thus obtained. We then confirmed whether Phantom numbers ② and ③ of Bone B, which we hypothesized would have regions of increased uptake, were appropriately detected. We measured the volumes of the detected regions and then compared the results with the designed values.

Evaluation using clinical data

Thirty-five subjects (17 males, 18 females) who were randomly selected from patients who underwent bone scintigraphy for the purpose of detecting bone metastasis at our hospital between April 2012 and June 2014 were used for evaluation. Their mean age was 61 ± 14 (range 30–80) years.

Data were obtained by performing whole-body planar and SPECT/CT imaging 3 h after intravenous injection of ^{99m}Tc-HMDP 740 MBq. When extracting bones from CT images, we avoided analytical errors caused by metal artifacts by excluding from our analysis patients who had internal metal and barium meal used in other types of X-ray examinations. All obtained image data were discussed by two specialists in nuclear medicine and were divided into two groups: 14 cases of normal uptake and 21 cases of abnormal uptake. The number of regions of abnormal uptake was 249. This study was approved by the Institutional Review Board of the Fujita Health University Hospital (no. HM15-630). All images were anonymized prior to use.

The normal uptake group among the clinical image data groups was used to confirm that bone region segmentation was appropriately performed. In our technique, regions in which abnormal uptake was detected were checked to determine whether the location on the original image was accurate and whether the number and sizes were accurate. To assess volume, specialists in nuclear medicine manually measured the volumes of the increased uptake regions as the gold standard. Subsequently, the correlation between the volume measurements made using our technique and the gold standard was evaluated.

To assess the accuracy of the regions identified as regions of increased uptake, we investigated the number of false positives per case and the sensitivity of our technique using the regions measured manually by the physician as true positives.

Thresholds for bone region segmentation using CT images were as follows: Th_{bone} was 90 and Th_{chest} was 60.

Results

Evaluation of results using phantoms

Images showing the results of evaluation using the three types of simulated bone phantoms are shown in Fig. 4b. The upper row shows the original images, and the lower row shows the images extracted using thresholding. For reference, CT images for Phantom ① are shown on the left. SPECT images for Phantoms ② and ③ from our design showed only one region into which a large amount of radioactive material was placed, based on our assumption that this would be a region of increased uptake. The volumes automatically calculated from the images of the three phantoms are shown in Table 1.

We did not detect a region of increased uptake in the SPECT image of Phantom ①, which we assumed would be a normal region. As designed, only one region each of increased uptake was extracted from Phantoms ② and ③. The radioactive concentration in the region of increased uptake in Phantom ②, which was close to normal, was found to be smaller than the bone region obtained from the CT image. In contrast to the designed *VI* value of 0.33, the actual measured value was 0.15, which was an underestimation. The *VI* for Phantom ③ was 0.33, as designed.

Table 1 Phantom results

Phantom	Modality	Calculated volume (cm³)			VI	
		Bone A	Bone B	Bone C	Designed value	Measured value
①	CT	22.45	22.38	22.25	0.00	0.00
	SPECT	0.00	0.00	0.00		
②	CT	22.12	22.26	22.03	0.33	0.15
	SPECT	0.00	10.26	0.00		
③	CT	22.52	22.48	22.35	0.33	0.33
	SPECT	0.00	22.30	0.00		

Evaluation results using clinical data

When our technique was applied to the images for assessment, we detected 177 of 249 regions of increased uptake, indicating a detection sensitivity of 71%, with the number of false positives per case being 8.19.

Representative detection results are shown in Fig. 5. In all cases, increased uptake within bone regions could be visually detected. Benign uptake in the upper and lower teeth and in the region near the sinuses was also accurately detected as regions of increased uptake.

The relationship between the volume values manually measured by the physician and the volumes of increased uptake regions detected using our technique is shown in Fig. 6a. Although the error increased in the cases that had numerous regions of abnormal uptake, the correlation coefficient was 0.868 ($p < 0.01$), indicating a good correlation between the manually measured volume and automated measured one.
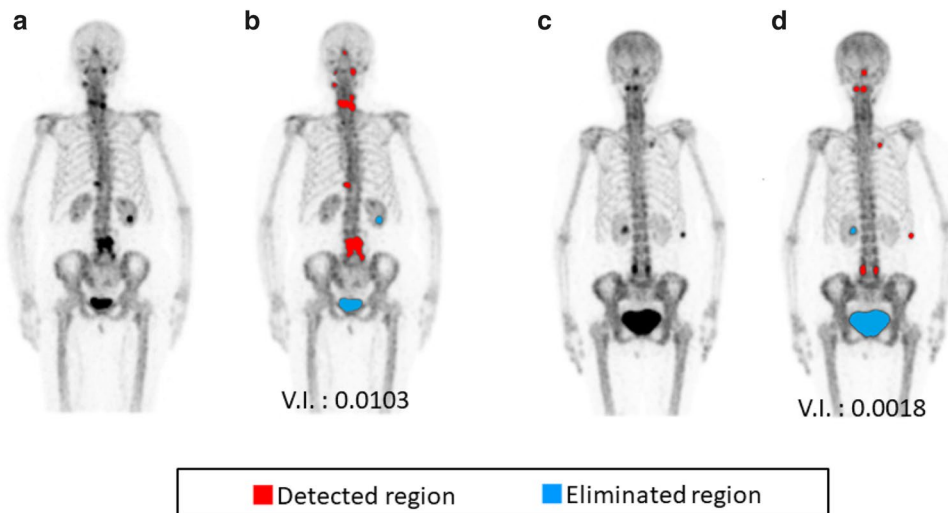

Fig. 5 Representative detection results. (Case 1: A 66-year-old female: Image reading report indicates uptake in nos. 6–7 cervical vertebrae, no. 11 thoracic vertebra, and no. 4 lumbar vertebra.) **a** Original image. **b** Image resulting from automated detection of increased uptake regions. (Case 2: A 73-year-old female: Image reading report indicated uptake in the left no. 10 costal cartilage transition zone and nos. 4–5 lumbar vertebrae.) **c** Original image. **d** Image resulting from automated detection of increased uptake regions. (Red, detected region; blue, region deleted as a false positive)
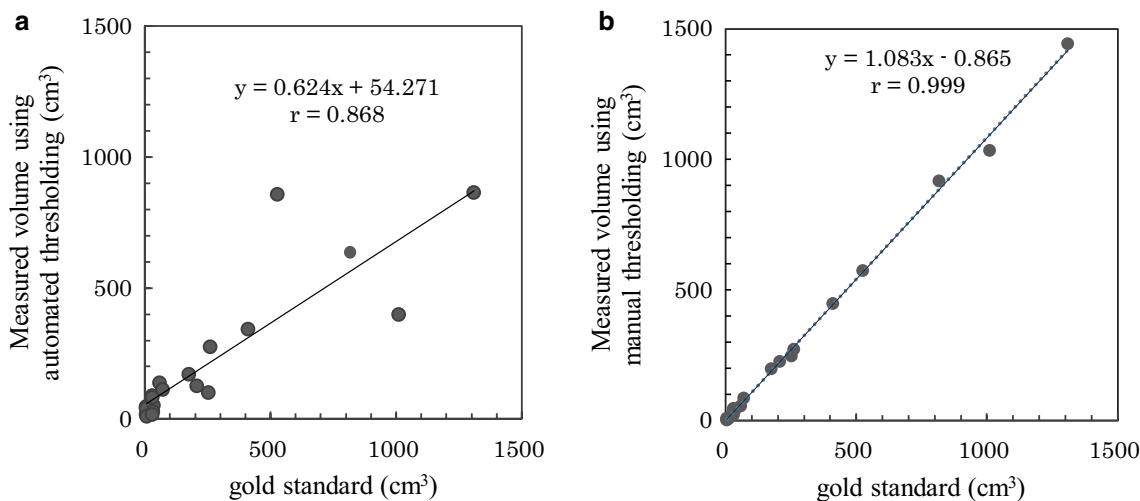

Fig. 6 Comparison of volumes detected using automated thresholds and manually determined thresholds and the gold standard method. **a** Proposed method and gold standard. **b** Manually determined threshold and gold standard

Cases that had numerous regions of abnormal uptake had larger errors. When the volumes measured manually by the physician were small, those detected by our technique were large, and vice versa. To investigate whether the threshold values were appropriately set, we compared the volumes for which the threshold value for detecting regions of increased uptake were manually adjusted using the manual measurements of the physician (Fig. 6b). The correlation coefficient for the results obtained by measuring with manually adjusted threshold value and the results obtained by the manual measurements of the physician was 0.999 ($p < 0.01$), indicating a detection sensitivity of 95%, with the number of false positives per case being 3.90.

Discussion

An automated detection method for the increased uptake regions using two-dimensional images has been proposed. However, no reports are available on the use of automated analysis with three-dimensional images. Using SPECT/CT images, it is possible to analyze the uptake regions three-dimensionally in conjunction with the bone information obtained from the CT images; remarkable improvement of accuracy is expected compared to two-dimensional analysis. Therefore, in this investigation, we developed an automated method for analyzing regions of increased uptake using whole-body SPECT/CT images and conducted a preliminary study on the detection capability of the proposed method using phantoms and clinical data. The results of both types of assessments indicated that only the use of data pertaining to bone regions obtained from SPECT images based on the bone regions extracted from CT images allowed accurate detection of increased uptake regions, indicating that our technique is effective.

Detection using phantoms indicated that our technique could correctly detect the number of regions with higher than normal uptake when using the simulated spine phantom that included three types (Normal, Normal×1.5, and Normal×3.7). However, in the case of Normal×1.5, which had a radioactive concentration close to that of the Normal type, the volume of the region of increased uptake was underestimated. We believe that this was likely caused by the spatial resolution of the SPECT device. SPECT images have a wider point spread function than CT images and thus a lower resolution [18, 19]. Regions in which uptake was higher than the detection threshold had wider edges, and as a result, the regions that exceeded the threshold were larger in reality. However, in the case of regions in which uptake exceeded the thresholds only slightly, uptake in the areas surrounding the region of interest was reduced by the point spread function and the volume that exceeded the threshold was reduced [20]. If the threshold values are decreased, false

positives will increase due to detection of normal regions as increased uptake regions. That is, there is a tradeoff between the accuracy of the detection volume and the number of false positives. A radical method of reducing this type of error would improve the resolution of the SPECT devices themselves. Currently, a method of resolution compensation that uses CT images in a clinical-use SPECT/CT device is being developed (xSPECT, Siemens, Germany [21]). We would like to perform additional verification checks with a device that uses this new technology. In this study, when extracting a bone region from a CT image, a threshold value with a fixed CT value was used. Since the volume value of the bone region is used for the calculation of the quantitative index (volume index), its accuracy is important. To evaluate the accuracy of segmentation, we prepared "reference images" of bone region by two specialists in nuclear medicine. They determined the optimal threshold of bone segmentation to make reference images. Jaccard index (JI) was calculated for the bone region extracted by the physician and the bone region extracted by the proposed method. JI is an index representing the degree of similarity between the reference image (A) and evaluation image (B), and is the ratio of the logic AND of A and B to the logic OR of A and B. The JI between the proposed method using the fixed threshold and bone volume manually extracted by the physician was 0.946. From this result, it was confirmed that a bone region could be extracted accurately using a fixed threshold when extracting the bone region from a CT image.

Application of our technique on the clinical data of 35 subjects indicated that the detection sensitivity was 71%, with 8.19 false positives per case. The correlation coefficient for our technique and manual measurements performed by a physician was high at 0.868. However, as shown by the regression line in Fig. 6a ($y = 0.624x + 54.271$), there were large errors in cases with numerous regions of abnormal uptake. When the volumes measured manually by the physician were small, the volumes detected by our technique were large and vice versa, indicating that a proportional systematic error occurred. The main reason for this is likely to be the fact that the setting of the threshold value used when measuring the volume of increased uptake regions was not appropriate. Thus, to investigate whether the threshold setting used was appropriate, we compared the volumes measured using manually adjusted thresholds with the manual measurements made by the physician for use in detecting increased uptake regions. The manual adjustment of the threshold value was set to a value considered to be optimal while visually checking the detection threshold value of increased uptake regions. In addition, bone region extraction and segmentation were performed automatically. The correlation coefficient for the measurement results obtained when the thresholds were manually adjusted and the results of the manual measurements made by the physician was

0.999, detection sensitivity 95%, and number of false positives per case 3.90. These results indicated that the method for determining the threshold is greatly affected by the accuracy of the analysis of the increased uptake regions. A previous study by Sadik et al. reported that automated methods for analyzing 2D images have a sensitivity of 90% [9, 11]. Compared with previously reported detection sensitivities, our technique has a low detection sensitivity of only 71%. However, the detection sensitivity when the thresholds were manually adjusted was quite high at 95%. To improve the results obtained by our technique, which handles data of higher dimensionality than that reported previously, it is necessary to make improvements, mainly in the method of setting thresholds. In the future, we would like to investigate and determine threshold derivation algorithms that use greater numbers of cases and additional parameters. In addition, to improve the analysis accuracy, we need to improve the algorithm that derives thresholding by conducting further assessments on higher numbers of cases.

In this study, we investigated the detection of increased uptake regions. However, in the future we would like to construct a diagnostic support system that can differentiate between benign and malignant regions of increased uptake based on data on anatomical location obtained from CT images.

In conclusion, we developed an automated method for detecting increased uptake regions using bone scintigraphy that utilizes both SPECT and CT images and performed a basic assessment of this method using phantoms and clinical data. The results of our assessment indicated that using data pertaining to the bone regions on SPECT images based on the bone regions extracted from CT images, the method could accurately detect regions of increased uptake, thereby confirming the efficacy of this method.

References

1. Bombardieri E, Aktolun C, Baum RP, Bishof-Delaloye A, Buscombe J, Chatal JF, et al. Bone scintigraphy: procedure guidelines for tumour imaging. Eur J Nucl Med Mol Imaging. 2003;30:BP99-BP106.
2. Koizumi M. Bone scintigraphy in bone metastasis. Radioisotopes. 1999;48:732–5.
3. Tamaki N, Manabe O. Textbook of clinical nuclear medicine. Japan: Bunkodo Co., Ltd.; 2016. pp. 128–52.
4. Koizumi M. Bone scintigraphy in oncology -essentials in diagnosis of bone metastasis. Tokyo: Mediculture Co., Ltd.; 2000. pp. 1–8.
5. Matsumoto T, Yoneda T. Cancer and bone. Tokyo: Medical Review Co., Ltd.; 2013. pp. 219–27.
6. Ono Y. Diagnosis of osseous metastasis by bone scintigraphy. Tokyo: Nankodo Co., Ltd.; 2002. pp. 31–49.
7. Yang HL, Liu T, Wang XM, Xu Y, Deng SM. Diagnosis of bone metastases: a meta-analysis comparing (18)FDGPET CT, MRI and bone scintigraphy. Euro Radiol. 2011;21:2604–17.
8. Savelli G, Maffioli L, Maccauro M, De Deckere E, Bombardieri E. Bone scintigraphy and the added value of SPECT (single photon emission tomography) in detecting skeletal lesions. Q. J Nucl Med. 2001;45:27–37.
9. Sadik M, Suurkula M, Höglund P, Järund A, Edenbrandt L. Quality of planar whole-body bone scan interpretations: a nationwide survey. Eur J Nucl Med Mol Imaging. 2008;35:1464–72.
10. Erdi YE, Humm JL, Imbriaco M, Yeung H, Larson SM. Quantitative bone metastases analysis based on image segmentation. J Nucl Med. 1997;38:1401–6.
11. Sadik M, Jakobsson D, Olofsson F, Ohlsson M, Suurkula M, Edenbrandt L. A new computer-based decision-support system for the interpretation of bone scans. Nucl Med Commun. 2006;27:417 – 23.
12. Sadik M, Hamadeh I, Nordblom P, Suurkula M, Höglund P, Ohlsson M, et al. Computer-assisted interpretation of planar whole-body bone scans. J Nucl Med. 2008;47:1958–65.
13. Sadik M, Suurkula M, Höglund P, Järund A, Edenbrandt L. Improved classifications of planar whole-body bone scans using a computer-assisted diagnosis system: multicenter, multiple-reader, multiple-case study. J Nucl Med. 2009;50:368 – 75.
14. Mitsui Y, Shiina H, Yamamoto Y, Haramoto M, Arichi N, Yasumoto H, et al. Prediction of survival benefit using an automated bone scan index in patients with castration-resistant prostate cancer. BJU Int. 2012;110:628 – 34.
15. Okutomi M, Ozawa S, Sato Y, Shimizu M, Fujiyoshi H, Hori O, et al. Digital image processing. Revised new ed. Tokyo: Computer Graphic Arts Society; 2015. p. 168 – 71, 186–7.
16. Suematsu Y, Yanada H. Image processing engineering. Revised ed. Japan: Corona Publishing Co., Ltd.,; 2000. pp. 128 – 29.
17. Matsumoto T, Yoshino M, Asano T, Uesugi K, Todoh M, Tanaka M. Monochromatic synchrotron radiation μCT reveals disuse-mediated canal network rarefaction in cortical bone of growing rat tibiae. J Appl Physiol. 2006;100:274–80.
18. Onishi H, Motomura N, Fujino K, Natsume T, Haramoto Y. Evaluation of commercial resolution recovery techniques in four state-of-the-art single photon emission computed tomography systems using a digital phantom model. Jpn J Radiol Technol. 2012;68:686–95.
19. Endo M, Iinuma T, Takenaka E. Measurement of CT-image resolution using a thin wire. Jpn J Radiol. 1980;40:43–51.
20. Onishi H, Ichihara T, Yamamoto T. Nuclear Medicine Technology. Revised 3rd ed. Japan: Ohmsha Co., Ltd.; 2016. pp. 123–4.
21. Vija AH. Introduction to xSPECT technology: evolving multimodal SPECT to become context-based and quantitative Siemens Healthcare White Paper. Illinois: Siemens Medical Solution; 2013.